


Drag-minimising bodies in confined Stokes flows

Edward M. Hinton¹  and Mohit P. Dalwadi^{2,3} 

¹School of Mathematics and Statistics, The University of Melbourne, Victoria 3010, Australia

²Mathematical Institute, University of Oxford, Oxford OX2 6GG, UK

³Department of Mathematics, University College London, London WC1H 0AY, UK

Corresponding author: Edward M. Hinton, edward.hinton@unimelb.edu.au

(Received 5 August 2025; revised 6 January 2026; accepted 16 January 2026)

Slow viscous flow around a fixed body generates a shape-dependent drag. We explore the drag-minimising shapes of bodies centred between two parallel plates in two-dimensional viscous flow. The channel width introduces a length scale so that the optimal profile is area-dependent. We solve the shape optimisation problem numerically over a wide range of areas. We also compute the optimal elliptical shapes and this identifies how these shapes should be slightly altered to reduce the drag with reductions of up to 3.8% attained at high areas. More broadly, we derive two properties of general optimal shapes within the confined flow: the magnitude of the surface vorticity is approximately (but not exactly) constant and the noses have sharp angles that are independent of area. For relatively small bodies, the optimal shape becomes identical to that in an unconfined geometry, but the drag is qualitatively different owing to the influence of confinement; within a channel, it is proportional to the inverse of the logarithm of the body area. At relatively large areas, the optimal body becomes long and its surface is approximately parallel to the channel boundaries, except in the vicinity of the noses. Using a lubrication approximation, we recast the optimisation problem as an Euler–Lagrange equation that is solved to determine the drag-minimising shape, finding that the drag is proportional to the body area in this regime.

Key words: drag reduction, low-Reynolds-number flows, variational methods

1. Introduction

Shape optimisation involves the selection of a body morphology that minimises or maximises some objective function, e.g. the drag on the body, subject to some constraint(s), e.g. a fixed body size or length. It has been observed that many shapes found in nature are optimal. Examples include fungi spores, which minimise drag (Roper *et al.* 2008), sperm and other active eukaryotic cells with flagella, which minimise the work

done while swimming (Lauga & Eloy 2013; Liu *et al.* 2025), and the outer hair cells in the mammalian ear, which minimise fluid dynamical resistance (Ciganović *et al.* 2017).

Elsewhere, the emergence and growth of biofilms has been shown to occur following optimal morphologies (Zhang *et al.* 2021), for example, in response to environmental forces (Nijjer *et al.* 2023). In addition, drug delivery can be improved by engineered design of the shape (Champion, Katare & Mitragotri 2007; Yu *et al.* 2024) and non-spherical shapes may sometimes be preferable (Banerjee *et al.* 2016).

Many of the aforementioned flows occur at low Reynolds numbers and are confined within a particular geometry. For definiteness, recall that the Reynolds number is $Re = \rho U \mathcal{L} / \mu$, where ρ is the fluid density, μ the dynamic viscosity, and U and \mathcal{L} are characteristic velocity and length scales, respectively. Stokes flows (i.e. flows with $Re = 0$) within unbounded domains are often substantially different to those within channels owing to the slow (algebraic) decay of the velocity field away from any disturbance in an infinite domain (Khalili & Liu 2017). Indeed, care must be taken when approximating problems where $0 < Re \ll 1$ with $Re = 0$ in domains of infinite extent, because inertia can become important in the far field. This typically involves matching an inner region of purely viscous flow with an outer region in which the inertia is incorporated (Proudman & Pearson 1957).

In this paper, we analyse the optimal shape in a two-dimensional channel flow between two parallel plates at zero Reynolds number. By ‘optimal’, we mean the shape that minimises the drag on the body with the constraint of fixed area. This problem has been studied for unbounded two-dimensional Stokes flows by Richardson (1995) who obtained the optimal body shape as well as the vorticity and drag on the body (both are in terms of $\log Re$ owing to the far-field behaviour).

In the limit of an unbounded fluid domain (both two-dimensional (2-D) and three-dimensional (3-D)) the drag-minimising body is also the shape that has constant vorticity on its surface (with a sign change across the axis of symmetry in 2-D) (Pironneau 1973). This result has been shown using a variational argument that relies upon the infinite extent of the domain (Pironneau 1973; Richardson 1995). We will show that, in contrast, the vorticity on the optimal body in a channel flow is approximately, but not exactly, constant. The deviation from constant vorticity is proportional to the square of the ratio of the thickness of the body to the channel width for small bodies and this result appears to be accurate even for non-small bodies. A corollary to the constant surface vorticity result in unbounded two-dimensional flow is that the drag-minimising body has a sharp nose at its front and back with an internal angle of 102.5° . We show that this remains the case in channel flow, with the angle unchanged, despite the vorticity not being constant.

Richardson (1995) calculated analytically the drag-minimising body in unbounded flow and showed that this shape is independent of the area of the body. This result does not translate into the channel problem since the channel width imposes a length scale. Hence, the optimal shape in this problem depends on the body area. In the limit of small area, the channel walls become less important and we show that the body shape does converge to Richardson’s optimal shape for unbounded flow.

There have been a range of studies on the numerical computation of resistance-minimising shapes in Stokes flows. An early study by Bourot (1974) used the constraint of constant angle at the noses to minimise the drag within a Stokes flow over a family of shapes, with the radial distance described by polynomials of $\sin \theta$ in terms of the polar angle θ . Another approach was presented by Zabarankin (2013) who focused on the more general problem of linear elasticity (the governing equations for Stokes flow are a special case of the Navier equations for linear elasticity). They used a different ansatz for the shape, which requires fewer terms to obtain an accurate solution (see

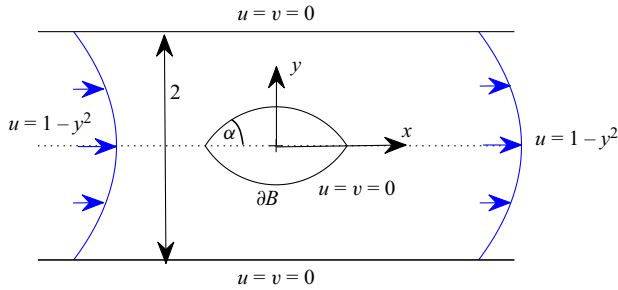


Figure 1. Schematic of the flow in dimensionless coordinates.

also Zabaranin & Nir 2011). Montenegro-Johnson & Lauga (2015) calculated the drag-minimising shapes with the alternative constraint of fixed surface area, whilst Mitchell & Spagnolie (2017) computed the body shapes that arise from erosion within a Stokes flow.

The paper is structured as follows. We formulate the problem of finding the minimal-drag body with fixed area centred within a Stokes flow in a two-dimensional channel in § 2. We describe and implement the numerical method for determining the Stokes flow and the optimal shape in § 3. To gain insight into the analysis of optimal bodies, we first consider the problem of finding the optimal ellipse in § 4, which reduces to a more straightforward one-parameter minimisation. We use asymptotic analysis to calculate the drag-minimising ellipse of small and large areas, which also identifies how these shapes can be improved when it comes to the general optimal body. We start considering properties of general optimal bodies in § 5, where we derive two key properties: the approximately (but not exactly) constant surface vorticity and the angle at the noses. These results are used to constrain and improve the numerical method. We then derive analytic results for the general optimal shape at small area and its associated drag in § 6. We also use lubrication theory to derive an Euler–Lagrange equation for the optimal shape at large areas. The solution shows excellent agreement with the full numerical results, even near the noses. Finally, we present concluding remarks in § 7.

2. Formulation

We analyse Stokes flow in a two-dimensional channel of thickness $2\mathcal{H}$ containing an isolated body, with the x - and y -coordinates parallel and perpendicular to the channel axis, respectively, with flow velocity denoted by (u, v) (see figure 1). There is no slip and no flux at the boundaries of the body and on the channel walls ($u = v = 0$). The flow is driven by a pressure gradient and, hence, the streamwise velocity profile is parabolic (Poiseuille flow) far upstream and far downstream of the body, with maximum velocity \mathcal{U} . The fluid has viscosity μ . We are interested in the shape that minimises the drag on the body, B , for a given area.

To non-dimensionalise the problem, we scale all velocities with \mathcal{U} and all lengths with the half-width of the channel, \mathcal{H} . The pressure scale is $\mu\mathcal{U}/\mathcal{H}$, whilst the drag scale is $\mu\mathcal{U}$. The dimensionless flow problem is summarised in figure 1.

Henceforth, all quantities are dimensionless. We introduce a stream function, ψ , such that

$$u = \frac{\partial\psi}{\partial y}, \quad v = -\frac{\partial\psi}{\partial x} \quad (2.1)$$

and the stream function satisfies the biharmonic equation

$$\nabla^4\psi = 0, \quad (2.2)$$

which is equivalent to the Stokes equations in two dimensions. Equation (2.2) is solved with no-slip and no-flux boundary conditions on the body boundary, ∂B ,

$$\psi = \frac{\partial \psi}{\partial n} = 0 \quad \text{for } (x, y) \in \partial B, \tag{2.3}$$

where $\partial/\partial n$ denotes the normal derivative. On the channel walls,

$$\psi = \pm \frac{2}{3}, \quad \frac{\partial \psi}{\partial y} = 0 \quad \text{on } y = \pm 1. \tag{2.4}$$

Far upstream and downstream, the Poiseuille flow is recovered with

$$\psi \rightarrow y - \frac{y^3}{3}, \quad \frac{\partial \psi}{\partial x} \rightarrow 0 \quad \text{as } x \rightarrow \pm \infty. \tag{2.5}$$

The stream function may then be computed for any body shape (see § 3.1). In what follows, it will be useful to have defined the vorticity, ω , and relate it to the pressure, p (which is its harmonic conjugate),

$$\omega = \frac{\partial v}{\partial x} - \frac{\partial u}{\partial y} = -\nabla^2 \psi, \quad \frac{\partial p}{\partial y} = \frac{\partial \omega}{\partial x}, \quad \frac{\partial p}{\partial x} = -\frac{\partial \omega}{\partial y}. \tag{2.6}$$

The drag on the body is given by

$$D(B) = \int_{\partial B} \sigma_{1j} n_j \, dS, \quad \text{where } \sigma_{ij} = -p \delta_{ij} + \frac{\partial u_i}{\partial x_j} + \frac{\partial u_j}{\partial x_i}, \tag{2.7}$$

and \mathbf{n} is the outward pointing unit normal. We are interested in the shape of the body that minimises the drag subject to the constraint of fixed area, which can be written as the following optimisation problem:

$$\min_B D(B) \quad \text{subject to} \quad \iint_B dx \, dy = A. \tag{2.8}$$

For each area, A , there is a different (i.e. generally non-similar) optimal shape, B .

We assume that a single body is the optimal body (rather than distributing the area over multiple bodies). We restrict our attention to bodies that have their centre of mass along $y = 0$ and we do not allow bodies that contact either of the channel walls. Under these restrictions and owing to the properties of Stokes flows, the optimal body B is symmetric about both $x = 0$ and $y = 0$.

Computing the drag will be key in the analysis and we note that (2.7) can be converted into an integral over the boundary of the truncated channel $(x, y) \in [-L, L] \times [-1, 1]$ using the divergence theorem, where $L \gg 1$ is sufficiently large that $\partial u/\partial x \approx 0$ at $x = \pm L$. The drag may then be written as

$$D = 2 \int_{-L}^L \left. \frac{\partial u}{\partial y} \right|_{y=1} dx + 2\Delta p, \tag{2.9}$$

where $\Delta p = [-p]_{-L}^L > 0$ is the pressure decrease from $x = -L$ to $x = +L$, and we have exploited the symmetry of the flow in both the x and y axes. We can then write the pressure as an integral of the vorticity along $y = 1$ by using (2.6) to obtain

$$D = 2 \int_{-L}^L \left(\left. \frac{\partial \omega}{\partial y} - \omega \right) \right|_{y=1} dx. \tag{2.10}$$

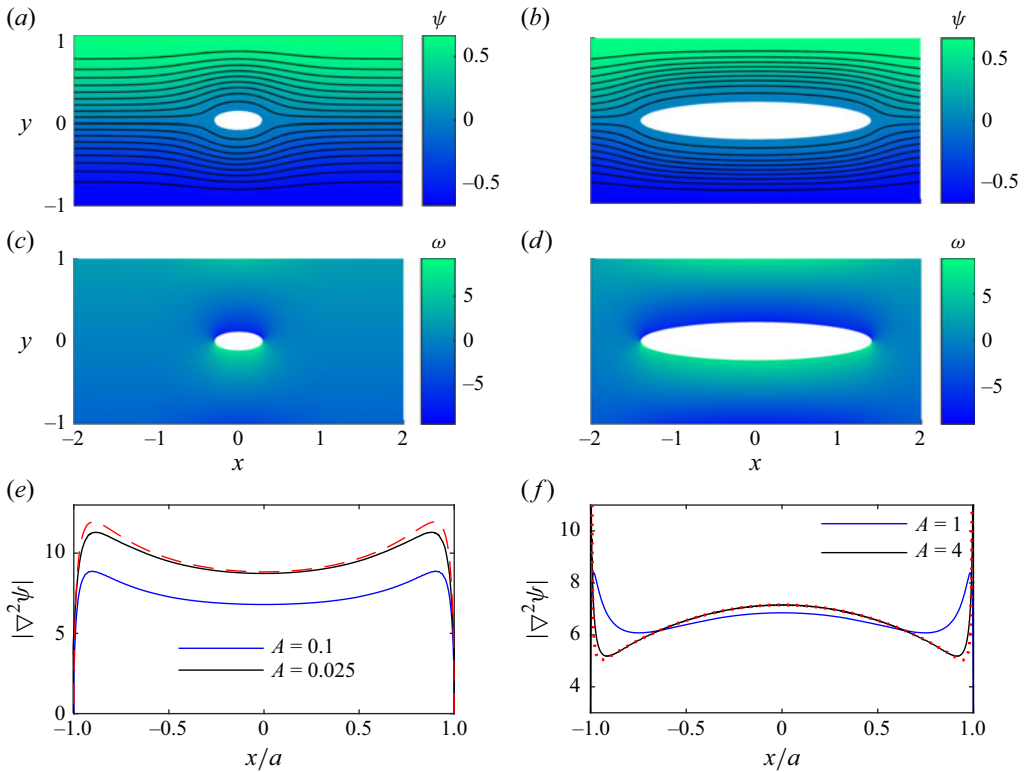


Figure 2. Flow past optimal elliptical bodies with different areas, A . (a,c) Streamfunction, ψ , and vorticity, ω , for $A = 0.1$, and (b,d) for $A = 1$. (e,f) Magnitude of the vorticity ($|\omega| = |\nabla^2\psi|$) on the ellipse boundary for different body areas. The red dashed line in panel (e) is the asymptotic result for small optimal ellipses (4.29), whilst the red dotted line in panel (f) is the asymptotic result for large optimal ellipses (4.37).

3. Numerical results

3.1. Numerical method to obtain the stream function

For a given body B , we solve the biharmonic equation (2.2) for the streamfunction $\psi(x, y)$ with boundary conditions (2.3)–(2.5) using MATLAB’s PDE toolbox. The computational domain is the rectangle $R = [-L, L] \times [-1, 1]$ with the body B removed, where $L \gg 1$ is chosen to be sufficiently large such that doubling L results in a change in the drag of less than 5×10^{-5} . For bodies with area of order unity, this condition is generally satisfied by using $L = 20$. Results for the flow around some elliptical bodies are shown in figure 2 (not all the computational domain is shown); these bodies are drag-minimising over the family of elliptical bodies. Results for the flow around some optimal bodies are shown in figures 3 and 4.

3.2. Shape optimisation

The minimisation of the drag under the constraint of a given fixed area (2.8) is achieved by parametrising the body shape using (Zabarankin 2013)

$$\zeta(t) = x(t) + iy(t) = C \sum_{j=0}^N \left(a_j \cos \frac{\pi t}{2} + ib_j \sin \frac{\pi t}{2} \right) T_j(2t - 1), \quad (3.1)$$

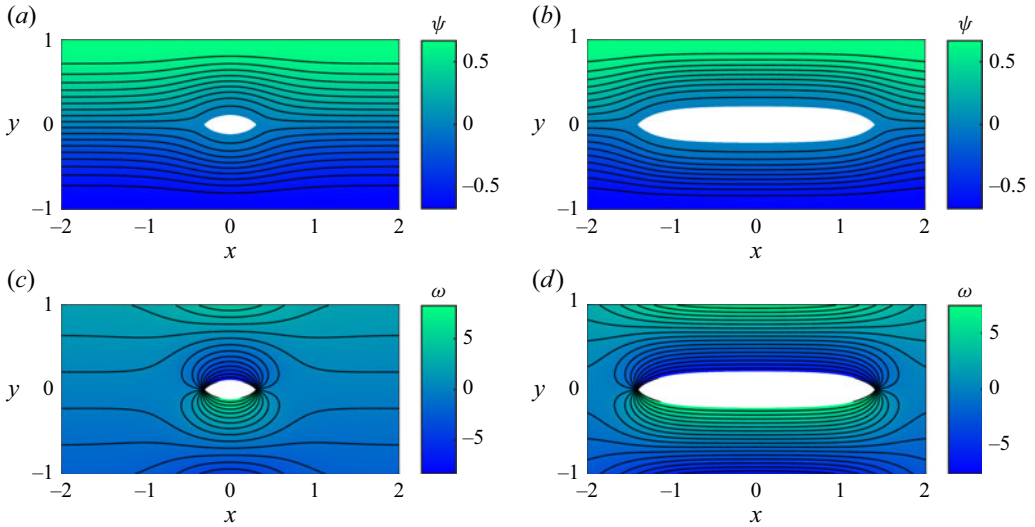


Figure 3. Flow past the general optimal body with areas (a,c) $A = 0.1$ and (b,d) $A = 1$: (a,b) streamfunction and streamlines; (c,d) vorticity.

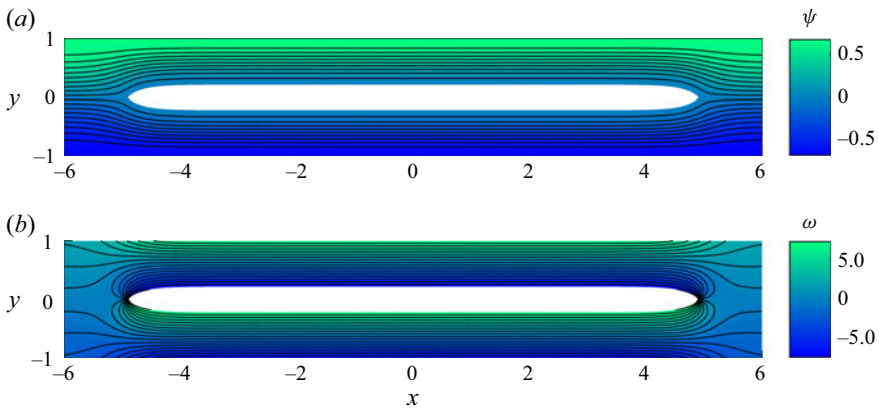


Figure 4. Flow past the general optimal body with area $A = 4$: (a) streamfunction and streamlines; (b) vorticity.

where $t \in [0, 1]$ and $T_j(\cdot)$ are the Chebyshev polynomials of the first kind and C is a normalisation constant that fixes the body area. Equation (3.1) gives the body shape in the positive quadrant and the rest of the shape is obtained via reflection.

For any integer $N \geq 0$, solution to the optimisation problem (2.8) involves finding the values of a_j and b_j that minimise the drag (note that there are $2N + 2 - 1 = 2N + 1$ free parameters owing to the fixed area condition, which manifests via determining C). For $N = 0$, the shape (3.1) is simply an ellipse. The representation (3.1) allows for any sharp angle at the noses provided that $N > 0$; we will use this explicitly in § 5.3.

The half-extent of the shape in the x and y directions is given by

$$a = \max(x) = C \sum_{j=0}^N a_j (-1)^j, \quad b = \max(y) = C \sum_{j=0}^N b_j. \quad (3.2)$$

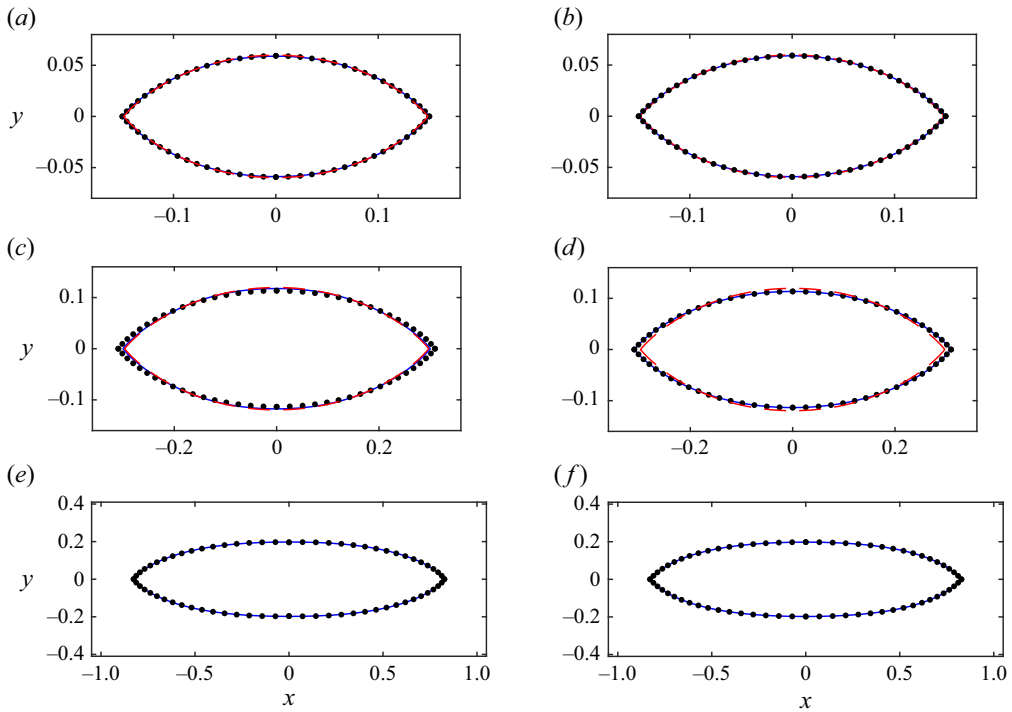


Figure 5. Optimal shapes with areas (a,b) $A=0.025$, (c,d) $A=0.1$, (e,f) $A=0.5$: result for a parameterisation (3.1) with (a,c,e) $N=2$; (b,d,f) $N=4$. The black dots are the shapes from the original optimisation approach (see § 3.2) and the blue lines are from the improved, constrained optimisation (see § 5.3). The red dashed lines in panels (a)–(d) are Richardson’s shape (6.1), accurate for $A \ll 1$. The shapes are not smooth at the two noses and the apices have internal angles less than π .

To obtain the drag-minimising shape, the strategy for a given area A uses alternating descent and proceeds by first finding the optimal elliptical shape ($N=0$), which is a one-parameter optimisation problem. We then increase $N \rightarrow N+2$, and vary each parameter a_j and b_j in turn seeking the smallest drag and using the elliptical body as the initial guess. This iteration continues until a desired tolerance is reached and we then increase N again. We generally continued until $N=6$, beyond which the reduction in the drag is typically less than 0.001%. Results for the optimal shapes of different areas are shown in figures 5 and 6 (black dots show the results of the simple ‘unconstrained’ optimisation described here).

4. Optimal elliptical bodies

It is instructive to initially consider the optimal elliptical body for a given area because of the relative simplicity of its optimisation. That is, while an ellipse is parametrised by two lengths, the constraint of fixed area makes this a one-parameter minimisation problem, solvable through numerical computation; see § 3. In addition, some of the features we will identify for optimal ellipses carry over to the general bodies and so the analysis provides insights into how the shape may be adjusted to reduce the drag whilst maintaining the area. The optimal elliptical bodies with areas $A=0.1$ and $A=1$ are shown in figure 2 along with the streamfunction and vorticity for the flow around the body. These optimal shapes

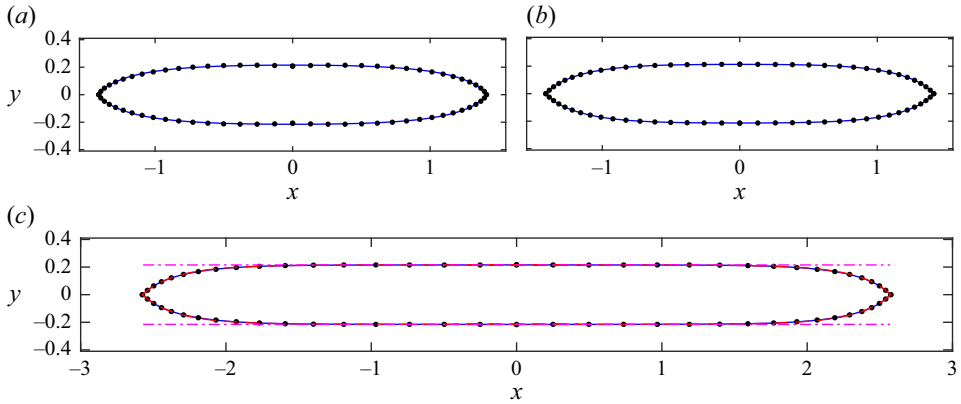


Figure 6. Optimal shape with area $A = 1$ using a parametrisation (3.1) with (a) $N = 2$ and (b) $N = 4$. (c) Optimal shape with area $A = 2$ and $N = 4$. The black dots are the shapes from the original optimisation approach (see § 3.2) and the blue lines are from the improved, constrained optimisation (see § 5.3). In panel (c), the magenta dash-dotted line is the leading-order asymptotic prediction (6.17), whilst the red dashes show the minimal drag shape calculated from lubrication theory; see also figure 12.

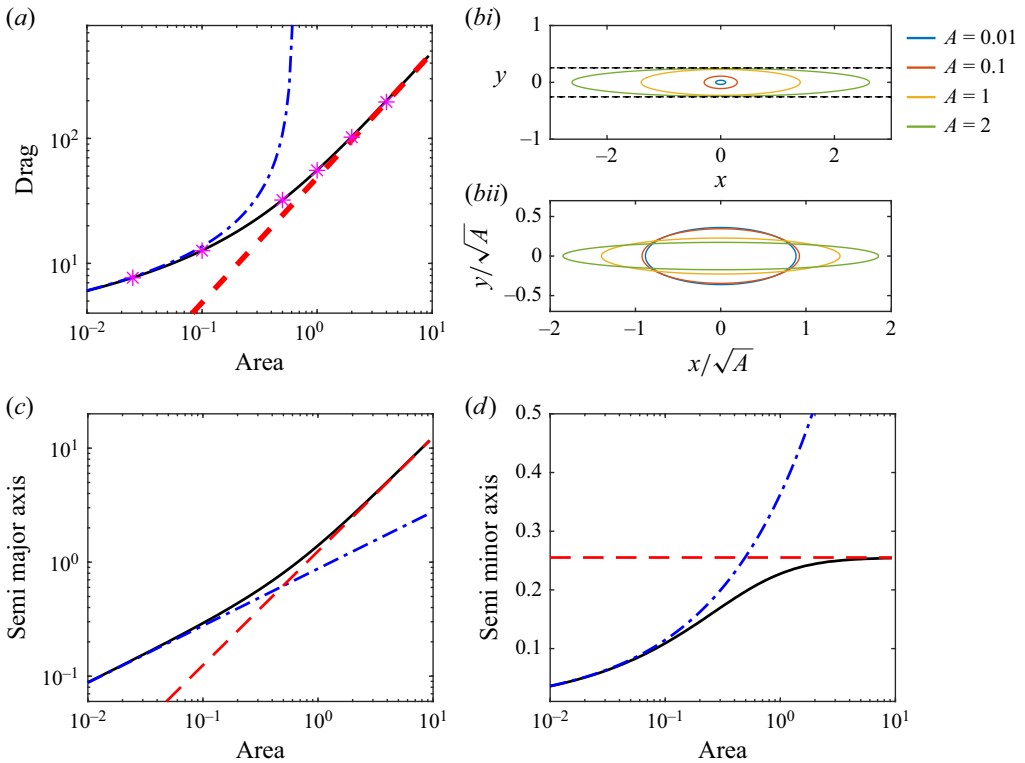


Figure 7. Optimal elliptical bodies. (a) Drag on optimal elliptical bodies of different areas computed numerically (black line). The small and large area asymptotic results ((4.24) and (4.39)) are shown as blue dash-dotted and red dashed lines, respectively. Magenta crosses show the minimal drag for the optimal shape, which is marginally less than the optimal ellipse. (bi) Optimal elliptical bodies with areas $A = 0.01, 0.1, 1, 2$ (the black dashed line is the asymptotic result for the body thickness for $A \gg 1$; (4.38)) and (bii) rescaled to have the same area. (c,d) Semi-major and semi-minor axes of optimal elliptical bodies and the corresponding asymptotic results for small area (blue dot-dashed lines, (4.26)) and large area (red dashed lines, (4.38)).

and the flow field were calculated numerically. The drag on optimal elliptical bodies is shown in figure 7(a) as a function of area.

In the rest of this section, we use asymptotic analysis to determine the optimal elliptical shapes as well as the associated drag and body surface vorticity for relatively small areas (§ 4.1) and relatively large areas (§ 4.2).

4.1. Small elliptical bodies

In this subsection, we calculate the optimal elliptical shape for $A \ll 1$; see also figure 2(a,b) for the corresponding numerical result. The optimal shape (and the associated flow field) are obtained via asymptotic analysis. The strategy is to construct the outer flow (away from the small body), which contains an undetermined coefficient in the streamfunction before determining the inner flow (which depends on the body shape) and then asymptotically matching the two solutions to determine the coefficients.

4.1.1. Outer solution

In the outer problem, the effect of the small body arises as a Stokeslet at the origin, without having to resolve its detailed shape. We write the streamfunction as

$$\psi_{out} = y - \frac{y^3}{3} + \hat{\psi}, \tag{4.1}$$

where the first two terms are associated with the far-field flow and the third term accounts for a Stokeslet at the origin superposed with its image terms to satisfy the boundary conditions on the walls (Happel & Brenner 1983; Crowdy & Davis 2013). The strength of the Stokeslet (which will end up being proportional to the leading-order drag on the small body) is shape-dependent and will be determined by matching to an appropriate inner region.

Away from the origin, we retain the biharmonic equation (2.2) $\nabla^4 \hat{\psi} = 0$. We seek a solution for $\hat{\psi}$ that satisfies the boundary conditions as $x \rightarrow \pm\infty$ and on the two plates, $y = \pm 1$ (ignoring the matching conditions as $x, y \rightarrow 0$ for now);

$$\hat{\psi} \rightarrow 0 \quad \text{as} \quad |x| \rightarrow \infty, \tag{4.2}$$

$$\hat{\psi} = \frac{\partial \hat{\psi}}{\partial y} = 0 \quad \text{on} \quad y = \pm 1. \tag{4.3}$$

To obtain the solution, we superpose the images of the Stokeslet and take a Fourier cosine transform in x ,

$$\Psi(k, y) = \int_0^\infty \hat{\psi}(x, y) \cos kx \, dx, \quad \hat{\psi}(x, y) = \frac{2}{\pi} \int_0^\infty \Psi(k, y) \cos kx \, dk. \tag{4.4}$$

The biharmonic equation (2.2) is then recast as

$$\frac{\partial^4 \Psi}{\partial y^4} - 2k^2 \frac{\partial^2 \Psi}{\partial y^2} + k^4 \Psi = 0. \tag{4.5}$$

We apply the boundary conditions at $y = \pm 1$ and in the far-field, and then invert the Fourier transform to obtain (Happel & Brenner 1983; Pozrikidis 1992; Crowdy & Davis 2013)

$$\hat{\psi} = \sum_{n=0}^\infty [B_{2n} f_{2n}(x, y) + C_{2n} g_{2n}(x, y)], \tag{4.6}$$

where

$$\begin{aligned}
 f_{2n}(x, y) &= \int_0^\infty k^{2n} \left[ye^{-k|y|} + \frac{(2k - 1 + e^{-2k})y \cosh ky - 2k \sinh ky}{\sinh 2k - 2k} \right] \frac{\cos kx}{k} dk, \\
 g_{2n}(x, y) &= \int_0^\infty k^{2n} \left[\frac{y}{|y|} e^{-k|y|} + \frac{2ky \cosh ky - (1 + 2k + e^{-2k}) \sinh ky}{\sinh 2k - 2k} \right] \cos kx dk,
 \end{aligned}
 \tag{4.7}$$

where we have exploited the symmetry properties of the flow in both the x and y directions.

To understand which terms in (4.6) are relevant to our analysis, it is helpful to understand the behaviour of the outer solution (4.6) for $r = \sqrt{x^2 + y^2} \ll 1$. The component functions (4.7) have the behaviour

$$f_{2n} \sim r^{1-2n} \quad \text{and} \quad g_{2n} \sim r^{-1-2n} \quad \text{as} \quad r \rightarrow 0.
 \tag{4.8}$$

We will later show that a small body of length scale $\varepsilon \ll 1$ (and inner radial coordinate $R = r/\varepsilon = O(1)$) has inner solution that grows as $O(R \log R)$ in its far-field. Hence, treating logarithms as $O(1)$ and matching between regions yields that the coefficients in (4.6) have asymptotic sizes of $B_{2n} = O(\varepsilon^{2n})$ and $C_{2n} = O(\varepsilon^{2n+2})$. Therefore, the leading-order version of (4.6) is

$$\hat{\psi} \sim B_0 f_0(x, y).
 \tag{4.9}$$

Using (4.9) in the outer stream function (4.1), we can deduce that the dominant behaviour of (4.1) for small r is

$$\psi_{out} \sim \left[1 + B_0 \left(\log \frac{1}{r} - \alpha_1 \right) \right] y,
 \tag{4.10}$$

where the constant α_1 is given by the following expression:

$$\alpha_1 = \int_0^\infty \frac{1 - 2k + 2k^2 - e^{-2k}}{k(\sinh 2k - 2k)} - \frac{e^{-k}}{k} dk \approx 0.4157.
 \tag{4.11}$$

With the outer solution in hand, we next obtain the inner solution for an ellipse and formally match this to the outer solution.

4.1.2. Inner solution for an elliptical body

For the inner problem in the vicinity of the ellipse, we write

$$x = \varepsilon X, \quad y = \varepsilon Y, \quad r = \varepsilon R,
 \tag{4.12}$$

where

$$\varepsilon = \sqrt{A/\pi} \ll 1,
 \tag{4.13}$$

and so ε represents the radius of a circle of equivalent area to the ellipse under consideration. The ellipse boundary is defined by

$$(X, Y) = (\tilde{a} \cos \eta, \tilde{b} \sin \eta), \quad \eta \in [0, 2\pi),
 \tag{4.14}$$

and so $\tilde{a}\tilde{b} = 1$, noting that these are related to the semi-minor and semi-major axes in (x, y) coordinates via $(a, b) = \sqrt{A/\pi} (\tilde{a}, \tilde{b})$. We also define elliptical coordinates

$$X = \tilde{c} \cosh \xi \cos \eta, \quad Y = \tilde{c} \sinh \xi \sin \eta,
 \tag{4.15}$$

where

$$\tilde{c} = \sqrt{\tilde{a}^2 - \tilde{b}^2}, \quad \frac{\tilde{a}}{\tilde{c}} = \cosh \xi_0, \quad \frac{\tilde{b}}{\tilde{c}} = \sinh \xi_0, \quad \xi_0 = \frac{1}{2} \log \frac{\tilde{a} + \tilde{b}}{\tilde{a} - \tilde{b}}, \quad (4.16)$$

and so the body boundary corresponds to $\xi = \xi_0$. In elliptical coordinates, the biharmonic equation becomes

$$\nabla^2 \left(\frac{1}{\cosh^2 \xi - \cos^2 \eta} \nabla^2 \psi \right) = 0, \quad \text{where} \quad \nabla^2 = \frac{\partial^2}{\partial \xi^2} + \frac{\partial^2}{\partial \eta^2}. \quad (4.17)$$

The solution with no-slip, no-flux on the body and the correct symmetry properties is determined by Shintani, Umemura & Takano (1983), and given as

$$\psi_{in} = E \left[(\xi - \xi_0) \sinh \xi - \sinh \xi_0 \cosh \xi_0 \sinh \xi + \sinh^2 \xi_0 \cosh \xi \right] \sin \eta, \quad (4.18)$$

for some constant E that is to be determined via matching with the outer solution.

4.1.3. Matching the inner and outer solutions

It is useful to note the large $R = \sqrt{X^2 + Y^2}$ behaviour of the elliptical coordinates,

$$\xi \sim \log \frac{2R}{\tilde{c}}, \quad \eta \sim \theta. \quad (4.19)$$

We expand the inner solution (4.18) in terms of the outer coordinates and find that the leading-order contributions are

$$\psi_{in} \sim E \left[\log \frac{2r}{\tilde{c}\varepsilon} - \xi_0 - \sinh \xi_0 \cosh \xi_0 + \sinh^2 \xi_0 \right] \frac{r}{\tilde{c}\varepsilon} \sin \theta. \quad (4.20)$$

Then, matching with the near-field outer solution (4.10) and comparing like terms furnishes the following two conditions:

$$-\frac{E}{\tilde{c}\varepsilon} = B_0, \quad (4.21)$$

$$\frac{E}{\tilde{c}\varepsilon} \left(\log \frac{2}{\tilde{c}\varepsilon} - \xi_0 - \sinh \xi_0 \cosh \xi_0 + \sinh^2 \xi_0 \right) = 1 - B_0 \alpha_1, \quad (4.22)$$

from which we find

$$-\frac{E}{\tilde{c}\varepsilon} = B_0 = \frac{-1}{\log \frac{1}{\varepsilon} - \alpha_1 - \frac{\tilde{b}}{\tilde{a} + \tilde{b}} + \log \frac{2}{\tilde{a} + \tilde{b}}}. \quad (4.23)$$

The drag on the body (2.7) may then be obtained,

$$D = \frac{4\pi}{\log \frac{1}{\varepsilon} - \alpha_1 - \frac{\tilde{b}}{\tilde{a} + \tilde{b}} + \log \frac{2}{\tilde{a} + \tilde{b}}}, \quad (4.24)$$

and by setting $\tilde{a} = \tilde{b} = 1$, we can recover the result for the drag on a circle (Takaisi 1955, 1956),

$$D_{circle} = \frac{4\pi}{\log \frac{1}{\varepsilon} - \alpha_1 - \frac{1}{2}} \approx \frac{4\pi}{\log \frac{1}{\varepsilon} - 0.9157}. \quad (4.25)$$

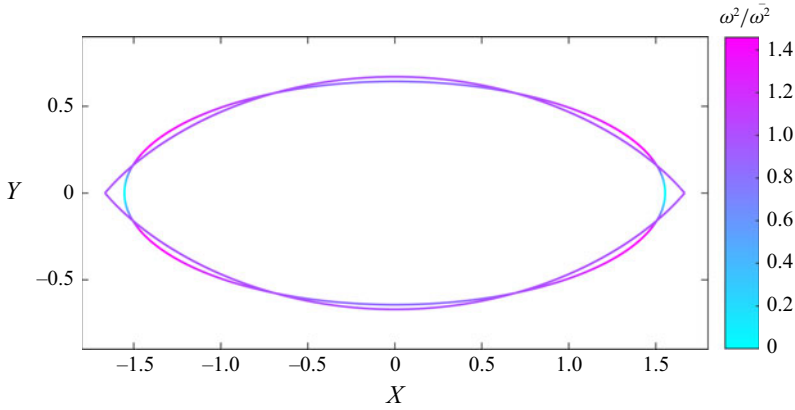


Figure 8. Comparison of the optimal elliptical shape (4.26) and the optimal general body shape (6.1) for small areas. The colour indicates the square of the vorticity on the body surface (relative to its mean), which is unity everywhere on the surface of the general optimal body and given by (4.29) for the ellipse.

The optimal ellipse (for $A \ll 1$) is obtained by minimising (4.24) subject to $\tilde{a}\tilde{b} = 1$, which furnishes

$$(a, b) = (\tilde{a}, \tilde{b})\sqrt{\frac{A}{\pi}} = \left(\sqrt{\sqrt{2} + 1}, \sqrt{\sqrt{2} - 1}\right)\sqrt{\frac{A}{\pi}} \approx (1.5538, 0.6436)\sqrt{\frac{A}{\pi}}. \tag{4.26}$$

This shape is shown in (X, Y) coordinates in figure 8.

The predictions (4.26) are compared with the numerical results for the optimal ellipse in figures 7(c) and 7(d). The leading-order aspect ratio of the optimal ellipse is $\sqrt{2} - 1 \approx 0.4142$, which is independent of ε , i.e. the area; see also figure 7(bii). The minimal drag can then be calculated from (4.24) and (4.26), yielding

$$D_{\text{ellipse}} = \frac{4\pi}{\log \frac{1}{\varepsilon} - \alpha_1 - 1 + \frac{1}{\sqrt{2}} + \frac{1}{2} \log(2\sqrt{2} - 2)} \approx \frac{4\pi}{\log \frac{1}{\varepsilon} - 0.8027}, \tag{4.27}$$

which shows good agreement with the numerical results for $A \ll 1$; see figure 7(a). The ratio of the drag on this optimal ellipse to the drag on a circle of the same area is

$$\frac{D_{\text{ellipse}}}{D_{\text{circle}}} \approx \frac{\log \frac{1}{\varepsilon} - 0.9157}{\log \frac{1}{\varepsilon} - 0.8027} \approx \frac{\log \frac{1}{A} - 0.6867}{\log \frac{1}{A} - 0.4607}. \tag{4.28}$$

Although this ratio approaches unity as $A \rightarrow 0$, the convergence is logarithmically slow. Indeed, the drag on the optimal ellipse is 12% less than the optimal circle for $A = 0.1$, 5% less for $A = 0.01$ and 3.5% less for $A = 0.001$. Equation (4.28) can also be interpreted as the small circle having the same drag as the small optimal elliptical body of 25.4% greater area.

The vorticity on the boundary of the optimal elliptical body is

$$\omega = \frac{2\tilde{a} \sin \eta}{\varepsilon(\tilde{a}^2 - \tilde{c}^2 \cos^2 \eta) \left(\log \frac{1}{\varepsilon} - 0.8027 \right)}, \quad (4.29)$$

which is compared with the numerical result for $A = 0.025$ in [figure 2\(e\)](#).

The body surface vorticity (4.29) vanishes at the upstream and downstream stagnation points ($\eta = 0^\circ, 180^\circ$), suggesting that the optimal general body requires a sharper apex angle. We formalise this observation later via variational analysis in §5.1 and via apex angle analysis in §5.2. The surface vorticity on the ellipse has local maxima at $\eta = \pm 22.5^\circ, \pm 157.5^\circ$; the vorticity is indicated by the colour of the ellipse in [figure 8](#). This figure also shows the small general optimal body and comparison suggests that at the locations on the ellipse near the local maxima of surface vorticity, the body must be ‘shrunk’ to obtain the optimal general body; see also the variational argument in §5. Likewise, the body should be ‘grown’ near the local minima of surface vorticity at the two ends of the ellipse.

4.2. Large elliptical bodies

In the regime of a large body, it is convenient to denote the body by

$$-a \leq x \leq a, \quad -h(x) \leq y \leq h(x), \quad (4.30)$$

where $h(x)$ is the shape of the boundary. We rescale the streamwise coordinate with

$$\chi = \frac{x}{a}, \quad (4.31)$$

with the body lying in $-1 \leq \chi \leq 1$. In the regime of large bodies ($A \gg 1$), the numerical results of [figures 7\(c\)](#) and [7\(d\)](#) indicate that the half-length of the optimal ellipse is proportional to the area, $a \propto A$, whilst its maximum thickness, $h(0)$, converges to a constant. Hence, the ratio of the channel thickness to the body length is proportional to $1/A \ll 1$ in this regime. As the two fluid gaps between the body and the channel walls are long and relatively thin, the flow is then predominantly in the horizontal direction with $v \ll u$. The exceptions are the two adjustment regions in the vicinity of the two apices in which the streamwise velocity in the centre of the channel transitions from unity to zero (or from zero to unity at the trailing end) over a distance $x = \mathcal{O}(1)$ or equivalently $\chi = \mathcal{O}(1/a)$ (e.g. Graebel 1965). We neglect the adjustment behaviour in these regions and assume that, away from the body, $u = 1 - y^2, v = 0$ in $|\chi| > 1$. Above and below the body, we deploy the lubrication approximation in $|\chi| < 1$ with

$$u = u_0(y; h(\chi)) + a^{-2}u_2(y; h(\chi)) + \mathcal{O}(a^{-4}), \quad (4.32)$$

$$v = a^{-1}v_0(y; h(\chi)) + a^{-3}v_2(y; h(\chi)) + \mathcal{O}(a^{-5}). \quad (4.33)$$

We use the higher-order lubrication equations to calculate velocities up to and including terms of order a^{-2} in the upper half of the channel, $h < y < 1$, which are given in [Appendix A](#) (see also Tavakol *et al.* 2017).

The drag on the body (2.10) may be written as

$$D = 2 \int_{-a}^a \left(\frac{\partial u}{\partial y} - \frac{\partial^2 u}{\partial y^2} \right) \Big|_{y=1} dx = 2a \int_{-1}^1 \left(\frac{\partial u}{\partial y} - \frac{\partial^2 u}{\partial y^2} \right) \Big|_{y=1} d\chi, \quad (4.34)$$

since by assumption, $u = 1 - y^2$ in $|x| > a$. This can be used to obtain the leading-order lubrication approximation for the drag,

$$D = 8a \int_{-1}^1 \frac{1+h}{(1-h)^3} d\chi \quad \text{where} \quad h(\chi) = b\sqrt{1-\chi^2}. \quad (4.35)$$

The vorticity is given by

$$\omega = -\frac{\partial u_0}{\partial y} + a^{-2} \left(\frac{\partial v_0}{\partial \chi} - \frac{\partial u_2}{\partial y} \right) + \mathcal{O}(a^{-4}), \quad (4.36)$$

and on the boundary of the body, this becomes

$$\omega(y=h) = -\frac{4}{(1-h)^2} + a^{-2} \left[\frac{8}{5(1-h)^2} \left(\frac{\partial h}{\partial \chi} \right)^2 + \frac{16}{15(1-h)} \frac{\partial^2 h}{\partial \chi^2} \right] + \mathcal{O}(a^{-4}). \quad (4.37)$$

For a large elliptical body, we seek the semi-major and semi-minor axes, a and b , which minimise the leading-order drag (4.35) subject to fixed area $ab\pi = A$. By writing $a = A/(b\pi)$, this becomes a one-parameter minimisation problem and the optimal choice, obtained via numerical quadrature, is

$$b \approx 0.2553, \quad a \approx 1.2469A, \quad (4.38)$$

which gives a minimal drag of

$$D \approx 38.9526, \quad a \approx 48.5705A. \quad (4.39)$$

The optimal large elliptical body has fixed semi-minor axis and is simply extended in the streamwise direction at larger areas; see figure 7(b). The leading-order asymptotic predictions for the drag on the optimal ellipse (4.39) and the semi-minor and semi-major axes of the optimal ellipse (4.38) are compared with the numerical results in figure 7, and there is good agreement for $A \geq 2$. We note that the next term in the drag on the ellipse is proportional to $\partial h/\partial \chi$ and $\partial^2 h/\partial \chi^2$, and so is technically singular as $\chi \rightarrow \pm 1$. Hence, a full and formal asymptotic treatment of this behaviour (which is beyond the scope of the present study) would require matching with a transition region near the noses when the lubrication equations start to break down, in which the flow is governed by the full Stokes equations.

The vorticity on the body (4.37) with $h = b\sqrt{1-\chi^2}$ is compared with the numerical result for the vorticity on the optimal ellipse for $A = 4$ in figure 2(f). The vorticity is singular at the apices, as expected, where the lubrication assumption breaks down (the vorticity must vanish at $\chi = \pm 1$ because each apex is a stagnation point).

5. Properties of general optimal bodies

The numerical results shown in figures 3–6 suggest that the vorticity is approximately constant over the body surface and that the angle at the two noses is area independent. In this section, we explicitly show that these are, in fact, two universal properties of general optimal bodies over all areas and we use the angle result to improve the computational efficiency of the numerical optimisation (§ 5.3).

5.1. Vorticity on the surface of an optimal body

In the case of uniform flow in an unbounded domain, the optimal body is the body that has constant vorticity on its boundary (Pironneau 1973; Richardson 1995; Zabaranin 2013). Here, we show that an optimal body in Poiseuille flow has approximately (but not exactly)

constant surface vorticity,

$$\omega^2 = \text{const.} + \mathcal{O}(b^2) \quad \text{on} \quad \partial B, \quad (5.1)$$

where b is the greatest half-thickness of the body and ∂B is the boundary of the body. There is a change of sign of ω across the centreline. This result is derived as follows.

First, from no-slip on the body boundary, $u_i = 0$ on ∂B , we find that

$$0 = \int_{\partial B} u_i \sigma_{ij} n_j \, dS. \quad (5.2)$$

We then consider a large rectangle $R = [-L, L] \times [-1, 1]$ with $L \gg 1$ where the boundary of R (which does not include the body boundary) is denoted by ∂R and the fluid domain is denoted by $R \setminus B$. Upon applying the divergence theorem, we obtain the relation

$$0 = - \iint_{R \setminus B} \frac{\partial u_i}{\partial x_j} \sigma_{ij} \, dx \, dy - \int_{\partial R} u_i \sigma_{ij} n_j \, dS, \quad (5.3)$$

where the unit normal points into the fluid domain. We use mass continuity and symmetry in the indices to recast the first integral as the viscous dissipation,

$$E_t \equiv \frac{1}{2} \iint_{R \setminus B} \left(\frac{\partial u_i}{\partial x_j} + \frac{\partial u_j}{\partial x_i} \right)^2 \, dx \, dy = \iint_{R \setminus B} \frac{\partial u_i}{\partial x_j} \sigma_{ij} \, dx \, dy. \quad (5.4)$$

The integrand in the second integral in (5.3) vanishes on $y = \pm 1$ owing to no-slip, which leaves the far-field contribution from the ends of the rectangle at $x = \pm L$, where $u = 1 - y^2$, $v = 0$ and $\partial p / \partial y = 0$ so that

$$- \int_{\partial R} u_i \sigma_{ij} n_j \, dS = \frac{4}{3} \Delta p, \quad (5.5)$$

where $\Delta p = [-p]_{-L}^L$ is the pressure decrease. Equation (5.3) then relates the viscous dissipation in the channel to the pressure drop,

$$\frac{4}{3} \Delta p = E_t. \quad (5.6)$$

In an unbounded domain, the drag on a body in Stokes flow is equal to the viscous dissipation in the fluid (e.g. Montenegro-Johnson & Lauga 2015), but in Poiseuille flow in a channel, the drag on the body also depends on the second moment of the x traction about the centreline of the body, which we denote by J . A similar manipulation to that already performed can be used to show that

$$J \equiv \int_{\partial B} y^2 \sigma_{1j} n_j \, dS = \frac{2}{3} \Delta p + 2 \int_{-L}^L \frac{\partial u}{\partial y} \Big|_{y=1} \, dx + \frac{16}{3} L. \quad (5.7)$$

Combining (5.6) and (5.7) with (2.9) furnishes

$$D = E_t - \frac{16}{3} L + J. \quad (5.8)$$

We now perturb the body via $\mathbf{x} \rightarrow \mathbf{x} + \delta c(s) \mathbf{n}$ with $\delta \ll 1$, where s denotes arclength, and we denote the small change in velocity by $\delta \tilde{\mathbf{u}}$ and in the stress tensor by $\delta \tilde{\boldsymbol{\sigma}}$. The perturbation in the drag (5.8) becomes

$$\delta \tilde{D} = \delta \tilde{E}_t + \delta \tilde{J}. \quad (5.9)$$

Here, the perturbations \tilde{E}_t and \tilde{J} are given by straightforward variational analysis (details of the calculations are given in [Appendix B](#); see also Pironneau 1973; Richardson 1995; Zabaranin 2013; Montenegro-Johnson & Lauga 2015),

$$\tilde{E}_t = 2 \int_{\partial B} c(s) \omega^2 \, dS, \quad \tilde{J} = \int_{\partial B} y^2 (\tilde{\sigma}_{1j} + \sigma_{1j} c(s)) n_j \, dS. \quad (5.10)$$

We introduce a cost function of the form

$$\mathcal{F} = D + \lambda (A_0 - A), \quad (5.11)$$

where λ is the Lagrange multiplier enforcing fixed area $A = A_0$, and we find that

$$0 = \tilde{\mathcal{F}} = \int_{\partial B} 2c\omega^2 + y^2 (\tilde{\sigma}_{1j} + \sigma_{1j}c) n_j - \lambda c \, dS. \quad (5.12)$$

Hence, as $y \rightarrow 0$ (i.e. in the limit of small bodies), the vorticity will be constant to leading order. Specifically, we can rewrite (5.12) as

$$0 = \int_{\partial B} 2c\omega^2 - \lambda c \, dS + \mathcal{O}(b^2). \quad (5.13)$$

The vorticity on the body hence satisfies

$$\omega^2 = \omega_0^2 + \mathcal{O}(b^2), \quad (5.14)$$

for some non-zero constant ω_0 . Over all areas, we show later (see § 6.2) that the optimal body has greatest thickness $b \leq 0.215$ and so $b^2 \leq 0.046$, and that the vorticity squared satisfies $\omega_0^2 \geq 42.189$. Thus, b^2 ends up being numerically small when compared with ω_0^2 . Moreover, it can be shown that the constant ω_0 is of $\mathcal{O}(1/b)$ as $A \rightarrow 0$ (i.e. as $b \rightarrow 0$) (Richardson 1995). Hence, the vorticity nowhere vanishes nor blows up on the body, which is important for analysing the apex; see § 5.2. The approximate condition (5.1) becomes exact in the limit $A \rightarrow 0$.

A shape with smooth boundary everywhere will always have a stagnation point with vanishing vorticity at the location on the boundary where the separating streamline meets the object. A stagnation point violates the optimality condition and so the optimal shape must have a sharp corner.

These results confirm that ω^2 is approximately (but not exactly) constant over the body surface. Equation (5.12) indicates that given a small non-optimal body shape (say an ellipse), the drag can generally be decreased by shrinking the body in regions where the vorticity on the boundary is larger than its mean and expanding the body in regions where the vorticity is small; e.g. [figure 8](#).

The drag can be written alternatively as

$$D = \frac{3}{2} E_t + 2 \int_{-L}^L \frac{\partial u}{\partial y} \Big|_{y=1} \, dx. \quad (5.15)$$

This description decomposes the drag into a contribution that is proportional to the dissipation and one that is proportional to the friction on the walls. For small bodies, the perturbation to the second term disappears i.e. \tilde{D} only has a contribution from the vorticity on the body squared (first term in (5.12)) for $A \ll 1$. Furthermore, if the channel wall boundary conditions were no flux and free slip ($v = \partial u / \partial y = 0$) rather than no flux and no slip ($u = v = 0$), then the condition of constant vorticity on the optimal body would be exact for all areas.

5.2. Optimal nose angle at the front and back is 102.5°

We now investigate the nose angle of the lowest-drag body in a channel. Whilst the argument we will use to determine the angle is based upon a local analysis, it relies upon the surface vorticity result from § 5.1, which takes into account the entire flow domain, including the channel walls.

Consider a polar coordinate system centred at the trailing edge of the body $(a, 0)$, so that

$$x = a + \tilde{r} \cos \tilde{\theta}, \quad y = \tilde{r} \sin \tilde{\theta}. \tag{5.16}$$

Locally to this trailing edge, the streamfunction takes the form (Moffatt 1964)

$$\psi = \tilde{r}^\lambda f_\lambda(\tilde{\theta}), \quad f_\lambda(\pm\beta) = f'_\lambda(\pm\beta) = 0. \tag{5.17}$$

where $\beta = \pi - \alpha$ and α is the half-angle at the leading and trailing edges; see figure 1. The vorticity on the body (locally to the trailing edge) is $-\nabla^2\psi \sim \tilde{r}^{\lambda-2}$. For the vorticity to be non-zero and non-singular as $\tilde{r} \rightarrow 0$ (from (5.1)), we require $\lambda = 2$. The $\tilde{\theta}$ dependence is then

$$f_2(\tilde{\theta}) = B_1 \sin 2\tilde{\theta} + B_2\tilde{\theta}, \tag{5.18}$$

to satisfy the biharmonic equation, where B_1 and B_2 are arbitrary constants. For a non-trivial solution that satisfies the boundary conditions, we require (Richardson 1995)

$$2\beta = \tan 2\beta, \tag{5.19}$$

which has the solution

$$\beta \approx 128.727^\circ, \quad \alpha \approx 51.273^\circ. \tag{5.20}$$

Therefore, the optimal nose angle is $2\alpha \approx 102.5^\circ$. Condition (5.20) is verified numerically in § 5.3 by computing the optimal shapes without using this constraint and comparing the results to constrained optimisation with the nose angle imposed; see also figures 5 and 6.

5.3. Applying constraints to the numerical optimisation

Our previous results can be used to reduce the computational effort of the numerical method (§ 3.2) for obtaining the optimal shape for $N \geq 2$. Namely, by using the results that the gradient at $x = 0$ vanishes owing to symmetry and that the gradient at the nose is fixed (see § 5.2), the number of free parameters in the shape optimisation is reduced by two. The condition that the noses are non-smooth and have fixed angle will be imposed as a constraint.

For the form of the shape given by (3.1), the derivatives with respect to t are given by

$$\frac{dx}{dt} = C \sum_{j=0}^N \left(-a_j \frac{\pi}{2} T_j(2t-1) \sin \frac{\pi t}{2} + 2a_j j U_{j-1}(2t-1) \cos \frac{\pi t}{2} \right), \tag{5.21}$$

$$\frac{dy}{dt} = C \sum_{j=0}^N \left(b_j \frac{\pi}{2} T_j(2t-1) \cos \frac{\pi t}{2} + 2b_j j U_{j-1}(2t-1) \sin \frac{\pi t}{2} \right), \tag{5.22}$$

where U_j are Chebyshev polynomials of the second kind.

At the nose ($t = 0$), the gradient of the boundary is fixed and so

$$-\tan \alpha = \frac{dy}{dx} = \frac{\sum_{j=0}^N b_j \frac{\pi}{4} (-1)^j}{\sum_{j=1}^N a_j j^2 (-1)^{j-1}}, \tag{5.23}$$

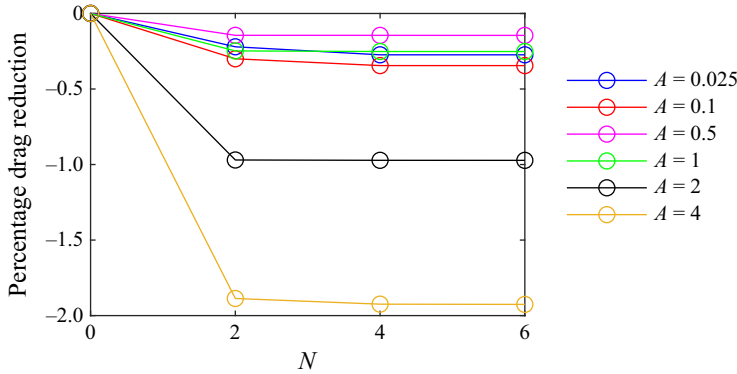


Figure 9. Drag reduction of optimal bodies relative to the optimal ellipse for different areas. The ellipse corresponds to the shape (3.1) with $N = 0$. Increasing N is associated with more degrees of freedom in the shape optimisation. For $N > 0$, the optimal body (and the associated drag) was calculated using the constrained approach described in § 5.3.

where α is the interior half-angle, given by (5.20). At the midpoint ($t = 1$), the gradient of the boundary vanishes giving

$$0 = \sum_{j=1}^N b_j j^2. \tag{5.24}$$

Hence, for $N \geq 2$, we impose

$$b_N = -\frac{1}{N^2} \sum_{j=1}^{N-1} b_j j^2 \tag{5.25}$$

as well as

$$a_N = \frac{\pi}{4} \cot \alpha \frac{(-1)^N}{N^2} \sum_{j=0}^N b_j (-1)^j - \frac{(-1)^N}{N^2} \sum_{j=1}^{N-1} a_j j^2 (-1)^j. \tag{5.26}$$

The constraints (5.25)–(5.26) reduce the number of free parameters to be determined in the optimisation process of § 3.2 from $2N + 1$ to $2N - 1$ and so the computational effort is lower. Differences between the optimisation results with and without these constraints for $N \geq 4$ are imperceptible; see figures 5 and 6. The drag on the optimal body for $N = 2, 4, 6$ is compared with the drag on the optimal ellipse ($N = 0$) for different areas in figure 9 (using the constraints (5.25)–(5.26) for $N \geq 2$). The change in drag between $N = 4$ and $N = 6$ was found to be less than 0.002 % for $A \leq 4$.

6. Asymptotic analysis of small and large optimal bodies

Figure 9 demonstrates that over a wide range of areas, the numerically calculated drag on the optimal body is less than on the optimal elliptical shape. The percentage reduction in drag going from the optimal ellipse to the optimal shape tends to be more significant at higher areas; see figure 9. In this section, we extend our analysis for the lowest-drag ellipse to the general problem of finding the lowest-drag shape with relatively small and large areas.

6.1. General optimal body of small area

Numerical results for the flow past the optimal body with $A = 0.1$ are shown in figure 3. Richardson (1995) calculated the optimal shape in an unbounded uniform Stokes flow, which is also the shape for which the vorticity has constant magnitude on its boundary. To construct the exact solution, Richardson (1995) conformally mapped the optimal body onto the unit circle and rewrote the three boundary conditions on the body boundaries (no-slip, no flux and constant vorticity) for this new domain. Richardson used a Goursat representation, which leaves two analytic functions (and the body shape) that must be determined by using the boundary conditions on the body surface and in the far-field. After various manipulations, the problem reduces to determining an analytic function that satisfies the correct jump conditions.

In the limit of small area, the optimal body in a channel has exactly constant surface vorticity (see § 5.1) and so it must have the same shape as Richardson’s solution. However, the drag on the optimal body in channel flow is different owing to wall effects. This difference can be understood by considering the asymptotic regions in the mathematical problem: in both the free-space and the channel flow configurations, the inner region for the flow around the optimal body has the same form, but the outer region is different (it must either account for inertia or it must account for the channel walls); see also § 1.

To understand the regime of confined flow past the small optimal body, we consider an inner coordinate system given by (4.12), with the body having area $A = \pi \varepsilon^2$ and where we define $Z = X + iY$. The body is given by

$$(X, Y) = (\mathcal{X}(s), \mathcal{Y}(s)), \tag{6.1}$$

and the shape of the optimal body in the positive quadrant is (Richardson 1995)

$$\mathcal{X}(s) = \sqrt{2} \int_0^\infty \frac{f'(k/2)}{f(k)} \sin(ks) dk, \quad \mathcal{Y}(s) = \sqrt{2} \int_0^\infty \frac{f(k/2)}{f(k)} \cos(ks) dk, \tag{6.2}$$

where $0 \leq s < \infty$ parametrises the body and $f(k) = k \cosh k - \sinh k$. The shape in the other three quadrants is obtained by symmetry. The area in (X, Y) coordinates is π and so the area in the original (x, y) coordinates is A . Equation (6.2) corresponds to the optimal shape with (in Richardson’s notation) dimensionless length scale $C = \pi/(2\sqrt{2})$. The half-extent and half-width of this body are

$$\max [\mathcal{X}(s)] = \frac{3\pi}{4\sqrt{2}} \approx 1.66608, \quad \max [\mathcal{Y}(s)] \approx 0.67065. \tag{6.3}$$

The optimal shape (6.1) is shown in figure 8, where it is compared with the optimal ellipse for $A \ll 1$.

The solution for the outer flow away from the optimal body has the same functional form as that in § 4.1.1 for the optimal elliptic body, with the difference in shape yielding different values for the matching constant B_0 . To determine its value, we note that the near-field expansion of the outer flow (4.10) is equivalent to the following complexified velocity:

$$u + iv = -B_0 \log r + \frac{B_0}{2} e^{2i\theta} - \left(\alpha_1 + \frac{1}{2} \right) B_0 + 1, \quad \text{as } r \rightarrow 0. \tag{6.4}$$

We now use (6.4) to determine B_0 by matching with the inner solution for Richardson’s optimal shape.

For the inner solution, we write the velocity using the Goursat representation as (Muskhelishvili 1977; Richardson 1995)

$$U + iV = \phi(Z) - Z\overline{\phi'(Z)} - \overline{\chi(Z)}. \tag{6.5}$$

To agree with the outer behaviour (6.4), we write the two analytic functions as (cf. Richardson 1995)

$$\phi(Z) = \frac{-B_0}{2} \log Z + \phi_0(Z), \quad \chi(Z) = \frac{B_0}{2} \log Z + Q + \chi_0(Z), \tag{6.6}$$

with $\phi_0(Z), \chi_0(Z) \rightarrow 0$ as $|Z| \rightarrow \infty$, and so the constant Q is obtained via matching (6.5) in the large- $|Z|$ limit with (6.4) to deduce

$$Q = -B_0 \left(\log \frac{1}{\varepsilon} - \alpha_1 - \frac{1}{2} \right) - 1. \tag{6.7}$$

Then, the solution of the inner flow problem (in which the magnitude of the body's surface vorticity is constant) furnishes (see Richardson 1995)

$$Q = \frac{-B_0}{2} \Lambda, \tag{6.8}$$

where

$$\begin{aligned} \Lambda &= 2 \log \frac{\pi}{4} + \frac{4}{\pi} G - 1 + \int_0^\infty \frac{(s^2 - \sinh s \tanh s) (s \sinh s - \cosh s + 1)}{s^2 \sinh s (s \cosh s - \sinh s)} ds \\ &\approx -0.23586, \end{aligned} \tag{6.9}$$

and

$$G = \sum_{n=0}^\infty \frac{(-1)^n}{(2n+1)^2} \approx 0.915965 \tag{6.10}$$

is Catalan's constant.

Equating (6.7) and (6.8) determines the constant

$$B_0 = \frac{-1}{\log \frac{1}{\varepsilon} - \alpha_1 - \frac{1}{2} - \frac{\Lambda}{2}} \approx \frac{-1}{\log \frac{1}{\varepsilon} - 0.7978}. \tag{6.11}$$

The drag is therefore

$$D \approx \frac{4\pi}{\log \frac{1}{\varepsilon} - 0.7978}, \tag{6.12}$$

which is a slight improvement on the optimal ellipse (4.27) with the drag proportional to $D = \mathcal{O}((\log \frac{1}{A})^{-1})$ as $A \rightarrow 0$ for both shapes. The prediction (6.12) is compared with the numerical results for the drag in figure 10(a).

The aspect ratio of this small optimal shape is 0.4025 and that of the small optimal ellipse is 0.4142; see figure 8 and also figure 10(b) for a comparison with the numerical results. The ratio of the drag on this optimal body to that on the optimal ellipse with the same area is

$$\frac{D_{optimal}}{D_{ellipse}} \approx \frac{\log \frac{1}{\varepsilon} - 0.8027}{\log \frac{1}{\varepsilon} - 0.7978} \approx \frac{\log \frac{1}{A} - 0.4607}{\log \frac{1}{A} - 0.4509}. \tag{6.13}$$

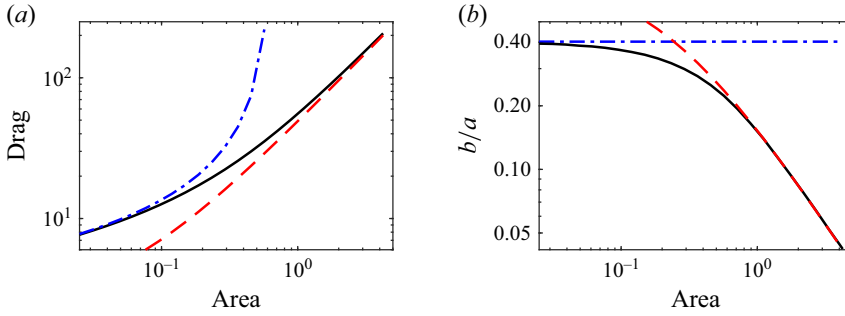


Figure 10. (a) Drag on the general optimal body as a function of area. Black lines show the numerical results, the blue dash-dotted line shows the small-area result (6.12) and red dashed lines shows the large-area result (6.28). (b) Aspect ratio of the general optimal body.

Equation (6.13) can be interpreted as the small optimal ellipse having the same drag as the small optimal general body of 0.98 % greater area. For $A = 0.1$, the optimal body has 0.53 % less drag than the optimal ellipse of the same area; for $A = 0.01$, it has 0.24 % less drag; and for $A = 0.001$, it has 0.15 % less drag than the optimal ellipse (see also figure 9).

Richardson’s shape (shown as red dashed lines) is compared with the numerically computed optimal shape in figure 5(a–d) and we see excellent agreement for $A = 0.025$ and reasonable agreement for $A = 0.1$. Figure 5(a–d) indicates that the first-order correction to Richardson’s shape, which accounts for modest wall effects, would make the optimal shape more slender.

The magnitude of the vorticity is constant (to leading order) on this optimal small-area body and is given by

$$|\omega| = \frac{-B_0}{2} \frac{\pi}{C\varepsilon} = \frac{\sqrt{2}}{\varepsilon \left(\log \frac{1}{\varepsilon} - 0.7978 \right)}. \tag{6.14}$$

Equation (6.14) can be compared with the vorticity magnitude on a small optimal ellipse (4.29), which varies with angle η , to estimate the four regions in which the ellipse has larger vorticity than the optimal body and so protrudes outside the optimal body (see figure 8). In the small- ε limit, the $\log 1/\varepsilon$ terms in the denominators dominate the small difference in the numerical constants 0.8027 and 0.7978, from which we may deduce that the regions of relatively higher body vorticity are ε -independent in the limit. Using this limit, in the positive quadrant, the ellipse has higher vorticity in the region given by angles that satisfy

$$14^\circ < \eta < 59^\circ, \tag{6.15}$$

with the other three regions obtained by symmetry.

6.2. Large bodies ($A \gg 1$)

Over most of their extent, optimal large bodies have constant thickness; see figure 4. Therefore, as a first approximation, we seek the rectangular body of length $2a$ and half-thickness h_0 that minimises the leading-order drag (according to the lubrication approximation; see § 4.2),

$$D = 8a \int_{-1}^1 \frac{1+h}{(1-h)^3} d\chi = \frac{16a(1+h_0)}{(1-h_0)^3} \tag{6.16}$$

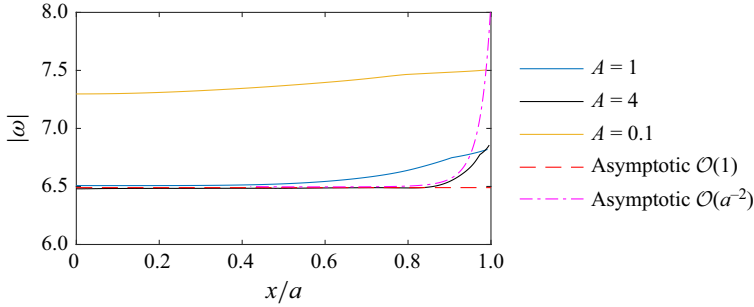


Figure 11. Magnitude of the vorticity on the surface of the optimal body for $A = 0.1, 1, 4$. The vorticity is approximately (but not exactly) constant; see § 5.1. The red dashed line shows the leading-order prediction for large A , (6.20), whilst the magenta dash-dotted line is the improved prediction from integrating (6.25) and using (4.37).

subject to fixed area, $4ah_0 = A$. This minimisation problem reduces to a single quadratic equation for h_0 with physical solution

$$h_0 = \frac{\sqrt{7} - 2}{3} \approx 0.2153, \tag{6.17}$$

which is independent of A and is slightly thinner at $x = 0$ than the optimal large ellipse, defined in (4.38). This prediction for the thickness shows excellent agreement with the numerical results away from the ends of the body; see the magenta dash-dotted line in figure 6(c). At the ends of the body, a more subtle treatment is required to account for $h = 0$ and the nose angle, which is discussed as follows.

The prediction (6.17) corresponds to a half-length of

$$a = \frac{3A}{4(\sqrt{7} - 2)} \approx 1.1614A, \tag{6.18}$$

and a minimal drag,

$$D = \left(\frac{536 + 208\sqrt{7}}{27} \right) a \approx 40.2339a, \quad D = \left(\frac{632 + 238\sqrt{7}}{27} \right) A \approx 46.7292A, \tag{6.19}$$

Comparing the minimal drag result (6.19) for the general optimal body to the equivalent result for the optimal ellipse (4.39) suggests a drag reduction of 3.8 %, which is significantly larger than the drag reduction for small bodies. The vorticity on the surface of this optimal body (away from the ends) is predicted to be

$$|\omega| = \frac{4}{(1 - h_0)^2} = \frac{32 + 10\sqrt{7}}{9} \approx 6.4953, \tag{6.20}$$

which is compared to the numerical results in figure 11.

To account for the ends of the body, we introduce the scaled coordinate $\zeta = 1 - a\chi = 1 - x$ (see § 4.2) and rewrite the drag as

$$D[h] = \int_0^a F(h, h', h'') \, d\zeta \tag{6.21}$$

$$= 16 \int_0^a \frac{1 + h}{(1 - h)^3} + \frac{h - 4}{15(1 - h)^2} \frac{\partial^2 h}{\partial \zeta^2} + \frac{3(h + 1)}{5(1 - h)^3} \left(\frac{\partial h}{\partial \zeta} \right)^2 \, d\zeta, \tag{6.22}$$

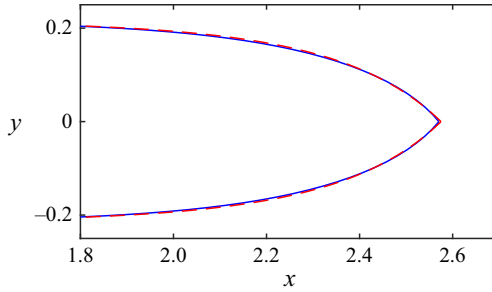


Figure 12. Comparison between the optimal shape computed with unconstrained optimisation (blue line) and the optimal shape obtained from lubrication theory (red dashed line from (6.25)) for $A = 2$ (the zoomed out version is shown in figure 6c).

where a prime denotes differentiation with respect to ζ and we have incorporated the next order term from the lubrication approximation; see Appendix A. Combining (6.21) with the fixed area constraint,

$$A[h] = \int_0^a G(h) d\zeta = 4 \int_0^a h d\zeta, \tag{6.23}$$

and writing $J = F - \lambda G$ (where λ is a Lagrange multiplier) furnishes the following Euler–Lagrange equation for the optimal shape

$$\frac{\partial J}{\partial h} - \frac{d}{d\zeta} \frac{\partial J}{\partial h'} + \frac{d^2}{d\zeta^2} \frac{\partial J}{\partial h''} = 0, \tag{6.24}$$

which must be solved subject to $h(a) = h_0$, $h'(a) = h''(a) = 0$ and $h(0) = 0$. The conditions at $\zeta = a$ determine λ and then (6.24) becomes

$$15 \left[2 + h - \frac{(2 + h_0)(1 - h)^4}{(1 - h_0)^4} \right] = 4 \left(\frac{\partial h}{\partial \zeta} \right)^2 (2h + 7) + 8 \frac{\partial^2 h}{\partial \zeta^2} (1 - h)(2 + h). \tag{6.25}$$

We integrate this ordinary differential equation for $h(\zeta)$ numerically, shooting from $\zeta = 0$ and selecting $h'(0)$ to ensure the boundary conditions as $\zeta \rightarrow a \gg 1$ are satisfied. We find that $h'(0) = 0.969$, which is a more acute nose angle than predicted by the complete nose analysis. Of course, the present analysis is not strictly valid at the nose because the lubrication approximation breaks down. Nonetheless, the solution, $h(\zeta)$, does an excellent job at predicting the shape; see the red dashed line in figures 6(c) and 12. It can also be used to approximate the vorticity on the body (4.37) (see figure 11 where it is compared with the numerical results for $A = 4$).

With the numerical solution to (6.25), we can calculate the area of this optimal body and its accompanying drag from (6.23) and (6.21),

$$A \approx 0.8610a - 0.2162, \quad D \approx 40.2339a - 6.2621, \tag{6.26}$$

where the leading-order terms are identical to the result for the optimal rectangle and, as expected, the rounding of the noses has reduced both the area and the drag (for a fixed value of the length a). The aspect ratio of the optimal body is given by

$$\frac{b}{a} \approx \frac{0.1853}{A + 0.2162}, \tag{6.27}$$

which is compared with the numerical results in [figure 10\(b\)](#). The drag can be written in terms of the area as

$$D \approx 46.7292A + 2.4365, \quad (6.28)$$

where the first term is as for the rectangle and the second term reflects the less efficient contribution from the noses. This prediction is compared with the numerical results in [figure 10\(a\)](#) and shows excellent agreement even for only moderate values of A . As for the ellipse, the drag is proportional to the area with $D = \mathcal{O}(A)$ as $A \rightarrow \infty$, but with a different prefactor.

7. Conclusion

We have used theoretical analysis and numerical computation to find the shape of body, centred within a Stokes flow in a two-dimensional channel, that minimises drag subject to the constraint of fixed area. The drag-minimising body is area-dependent, and asymptotic predictions have been obtained for bodies that are small and large relative to the channel width. The magnitude of the surface vorticity is approximately constant over the lowest-drag body and it becomes exactly constant when the channel walls have negligible influence. In addition, the result that the nose angle of the lowest-drag two-dimensional body in unbounded Stokes flow is 102.5° has been generalised to a confined channel geometry and the angle has been shown to be area-independent.

For relatively large optimal bodies in a channel, the body boundaries must be parallel to the channel walls with the ratio of the body thickness to the channel thickness given by $1/3(\sqrt{7} - 2)$ over most of the body's extent except near the noses, which reduce the drag-efficiency of the body. Small optimal bodies have shape that is independent of the wall effects, but the drag is influenced by the confinement.

The present study could be usefully extended in various ways. Straightforward future studies could analyse the three-dimensional optimal body within an axisymmetric pipe flow or the optimal body in the case of channel walls with free slip (for which the surface vorticity will be constant, as we have shown). Of relevance to biofilms is the interaction between growth of the body fuelled by nutrients within the fluid and the local shear stress tending to limit the expansion. The steady state optimal body in this case will be asymmetric in the fore–aft direction owing to the depletion of nutrients towards the trailing portion of the body (e.g. in biofilms; see [Pearce *et al.* 2019](#)). For small bodies, one could achieve lower drag by placing the body away from the centreline and even lower drag by adhering the body's mass to one of the channel walls. This problem would be a straightforward adaptation of the present study.

Acknowledgements. This research was supported by The University of Melbourne's Research Computing Services and the Petascale Campus Initiative. The authors are grateful to the Department of Mathematics at University College London for hosting the visit of E.M.H. in 2024 when this research was initiated.

Funding. E.M.H. acknowledges support from the Australian Research Council through a Discovery Early Career Researcher Award (DECRA:DE240100755).

Declaration of interests. The authors report no conflict of interest.

Appendix A. Lubrication theory

This appendix presents the calculations for the velocity (u, v) using the lubrication approximation for long bodies ($a \gg 1$, i.e. $A \gg 1$). The Stokes equations may be written

as (see also Tavakol *et al.* 2017)

$$a^{-1} \frac{\partial u}{\partial \chi} + \frac{\partial v}{\partial y} = 0, \tag{A1}$$

$$a^{-2} \frac{\partial^2 u}{\partial \chi^2} + \frac{\partial^2 u}{\partial y^2} = \frac{\partial \mathcal{P}}{\partial \chi}, \tag{A2}$$

$$a^{-4} \frac{\partial^2 v}{\partial \chi^2} + a^{-2} \frac{\partial^2 v}{\partial y^2} = \frac{\partial \mathcal{P}}{\partial y}, \tag{A3}$$

where \mathcal{P} is a rescaled pressure. The boundary conditions are $u = v = 0$ at $y = h(\chi)$, 1 and $\int_{h(\chi)}^1 u \, dy = 2/3$. The velocities are then written in the forms (4.32) and (4.33). At leading order,

$$\frac{\partial u_0}{\partial \chi} + \frac{\partial v_0}{\partial y} = 0, \tag{A4}$$

$$\frac{\partial^2 u_0}{\partial y^2} = \frac{\partial \mathcal{P}}{\partial \chi}, \tag{A5}$$

$$0 = \frac{\partial \mathcal{P}}{\partial y}. \tag{A6}$$

The solution that gives the correct flux and satisfies the boundary conditions is

$$u_0 = \frac{4(y-h)(1-y)}{(1-h)^3}. \tag{A7}$$

The cross-channel leading-order velocity term, v_0 , may then be calculated from (A4) to give

$$v_0 = \frac{4(y-h)(1-y)^2}{(1-h)^4} \frac{\partial h}{\partial \chi}. \tag{A8}$$

At next order, the Stokes equations become

$$\frac{\partial u_2}{\partial \chi} + \frac{\partial v_2}{\partial y} = 0, \tag{A9}$$

$$\frac{\partial^2 u_2}{\partial y^2} - \frac{\partial \mathcal{P}_2}{\partial \chi} = -\frac{\partial^2 u_0}{\partial \chi^2}, \tag{A10}$$

$$\frac{\partial^2 v_0}{\partial y^2} = \frac{\partial \mathcal{P}_2}{\partial y}, \tag{A11}$$

and the boundary conditions on u_2 are no slip at $y = h$, 1 and no net flux through the channel. The last equation is integrated to obtain

$$\mathcal{P}_2 = -\frac{\partial u_0}{\partial \chi} + c_2(\chi) \tag{A12}$$

for some function of integration $c_2(\chi)$. Equation (A10) is integrated twice and upon applying the boundary conditions and the flux condition to determine $c_2(\chi)$, we obtain

$$u_2 = \frac{(y-h)(1-y)(-16 + 50y - 30y^2 + 10hy - 18h + 4h^2)}{15(1-h)^4} \frac{\partial^2 h}{\partial \chi^2} \tag{A13}$$

$$+ \frac{(y-h)(1-y)(-28 + 80y - 40y^2 - 24h + 12h^2)}{5(1-h)^5} \left(\frac{\partial h}{\partial \chi} \right)^2. \tag{A14}$$

Appendix B. Variational argument for the surface vorticity

B.1. Normal derivative of the velocity at the body boundary

We first show that

$$\frac{\partial \mathbf{u}}{\partial n} = \omega \mathbf{t} \quad \text{on } \partial B, \quad (\text{B1})$$

where \mathbf{t} is the tangent vector to ∂B . Since $u = v = 0$ on the body, we have $\mathbf{t} \cdot \nabla \mathbf{u} = 0$, which can be rewritten as

$$n_y \frac{\partial \mathbf{u}}{\partial x} = n_x \frac{\partial \mathbf{u}}{\partial y}, \quad (\text{B2})$$

where $\mathbf{n} = (n_x, n_y)$ and $\mathbf{t} = (-n_y, n_x)$. We write

$$\frac{\partial \mathbf{u}}{\partial n} = \left(\frac{\partial u}{\partial x} n_x + \frac{\partial u}{\partial y} n_y, \frac{\partial v}{\partial x} n_x + \frac{\partial v}{\partial y} n_y \right) \quad (\text{B3})$$

$$= \left(-\frac{\partial v}{\partial y} n_x + \frac{\partial u}{\partial y} n_y, \frac{\partial v}{\partial x} n_x - \frac{\partial u}{\partial x} n_y \right) \quad (\text{B4})$$

$$= \left(-\frac{\partial v}{\partial x} n_y + \frac{\partial u}{\partial y} n_y, \frac{\partial v}{\partial x} n_x - \frac{\partial u}{\partial y} n_x \right) \quad (\text{B5})$$

$$= \omega \mathbf{t}, \quad (\text{B6})$$

where we have used continuity to obtain the second line and (B2) to obtain the third.

B.2. Stress vector on the body

Next, we show that

$$\boldsymbol{\sigma} \mathbf{n} = -p \mathbf{n} + \omega \mathbf{t} \quad \text{on } \partial B. \quad (\text{B7})$$

The pressure term in (B7) is straightforward to obtain from the definition of the stress in (2.7) and so we focus on the rate-of-strain term

$$\left(\frac{\partial u_i}{\partial x_j} + \frac{\partial u_j}{\partial x_i} \right) n_j. \quad (\text{B8})$$

The first term is $(\partial u_i / \partial x_j) n_j = (\partial \mathbf{u} / \partial n)$, whilst the second vanishes owing to (B2) and mass continuity. We then apply (B1) to obtain the required result.

B.3. Change in the terms in the drag following a small variation in the body

The dissipation is defined by

$$E_t \equiv \frac{1}{2} \iint_{R \setminus B} \left(\frac{\partial u_i}{\partial x_j} + \frac{\partial u_j}{\partial x_i} \right)^2 dx dy, \quad (\text{B9})$$

where $R \setminus B$ is the fluid region exterior to the body within the truncated channel $|x| \leq L (\gg 1)$, $|y| \leq 1$. The drag (5.8) also contains the term J ;

$$J \equiv \int_{\partial B} y^2 \sigma_{1j} n_j dS. \quad (\text{B10})$$

We are interested in the variation in the quantities E_t and J following a change to the body boundary of $\mathbf{x} \rightarrow \mathbf{x} + \delta c(s) \mathbf{n}$ with $\delta \ll 1$, where s denotes arclength, and we denote the small change in velocity by $\delta \tilde{\mathbf{u}}$ and in the stress tensor by $\delta \tilde{\boldsymbol{\sigma}}$. Similarly, the small changes in E_t and J are denoted by $\delta \tilde{E}_t$ and $\delta \tilde{J}$.

A Taylor expansion of the velocity field at the body boundary, $(\mathbf{u} + \delta\tilde{\mathbf{u}})(\mathbf{x} + \delta c(s)\mathbf{n}) = \mathbf{0}$ yields (Montenegro-Johnson & Lauga 2015)

$$\tilde{\mathbf{u}} = -c(s)\frac{\partial\mathbf{u}}{\partial n} \quad \text{on } \partial B. \quad (\text{B11})$$

We begin with the dissipation for which the variation is

$$\tilde{E}_t = \iint_{R\setminus B} \left(\frac{\partial u_i}{\partial x_j} + \frac{\partial u_j}{\partial x_i} \right) \left(\frac{\partial \tilde{u}_i}{\partial x_j} + \frac{\partial \tilde{u}_j}{\partial x_i} \right) dx dy. \quad (\text{B12})$$

Using the divergence theorem and the boundary conditions on the channel walls and in the far field, this can be rewritten as

$$\tilde{E}_t = -2 \iint_{R\setminus B} \tilde{u}_i \left(\frac{\partial^2 u_i}{\partial x_j \partial x_j} + \frac{\partial^2 u_j}{\partial x_i \partial x_j} \right) dV - 2 \int_{\partial B} \tilde{u}_i \left(\frac{\partial u_i}{\partial x_j} + \frac{\partial u_j}{\partial x_i} \right) n_j dS. \quad (\text{B13})$$

The second term in the first integral vanishes owing to continuity, whilst the first term can be rewritten in terms of the pressure gradient. In addition, in the second integral, we use (B11) to obtain

$$\tilde{E}_t = -2 \iint_{R\setminus B} \tilde{u}_i \frac{\partial p}{\partial x_i} dV + 2 \int_{\partial B} c(s) \frac{\partial u_i}{\partial n} \left(\frac{\partial u_i}{\partial x_j} + \frac{\partial u_j}{\partial x_i} \right) n_j dS. \quad (\text{B14})$$

The first integral on the right-hand side of (B14), using (B1), (B11) and continuity of u , can be written as

$$2 \int_{\partial B} p \tilde{u}_i n_i dS = -2 \int_{\partial B} p c(s) \mathbf{n} \cdot \frac{\partial \mathbf{u}}{\partial n} dS = 0. \quad (\text{B15})$$

In Appendix B.2, we showed that

$$\left(\frac{\partial u_i}{\partial x_j} + \frac{\partial u_j}{\partial x_i} \right) n_j = \frac{\partial u_i}{\partial n}, \quad (\text{B16})$$

which we substitute into (B14) to obtain

$$\tilde{E}_t = 2 \int_{\partial B} c(s) \frac{\partial u_i}{\partial n} \frac{\partial u_i}{\partial n} dS = 2 \int_{\partial B} c(s) \omega^2 dS, \quad (\text{B17})$$

where the second equality comes from (B1). This expression provides the result in (5.10).

The variation to J is

$$\delta \tilde{J} = \int_{\partial(B+\delta\tilde{B})} y^2 (\sigma_{1j} + \delta\tilde{\sigma}_{1j}) n_j dS - \int_{\partial B} y^2 \sigma_{1j} n_j dS, \quad (\text{B18})$$

where $\partial(B + \delta\tilde{B})$ is the boundary of the perturbed body. This is recast as

$$\delta \tilde{J} = \int_{\partial B} y^2 \delta\tilde{\sigma}_{1j} n_j dS + \int_{\partial B} y^2 \sigma_{1j} n_j \delta c(s) dS + \mathcal{O}(\delta^2), \quad (\text{B19})$$

where the second term accounts for the change in the surface geometry. The result (5.10) follows.

REFERENCES

- BANERJEE, A., QI, J., GOGOI, R., WONG, J. & MITRAGOTRI, S. 2016 Role of nanoparticle size, shape and surface chemistry in oral drug delivery. *J. Control. Release* **238**, 176–185.
 BOURROT, J.-M. 1974 On the numerical computation of the optimum profile in Stokes flow. *J. Fluid Mech.* **65** (3), 513–515.

- CHAMPION, J.A., KATARE, Y.K. & MITRAGOTRI, S. 2007 Particle shape: a new design parameter for micro- and nanoscale drug delivery carriers. *J. Control. Release* **121** (1–2), 3–9.
- CIGANOVIĆ, N., WOLDE-KIDAN, A. & REICHENBACH, T. 2017 Hair bundles of cochlear outer hair cells are shaped to minimize their fluid-dynamic resistance. *Sci. Rep.* **7** (1), 3609.
- CROWDY, D.G. & DAVIS, A.M.J. 2013 Stokes flow singularities in a two-dimensional channel: a novel transform approach with application to microswimming. *Proc. Roy. Soc. A* **469** (2157), 20130198.
- GRAEBEL, W.P. 1965 Slow viscous shear flow past a plate in a channel. *Phys. Fluids* **8** (11), 1929–1935.
- HAPPEL, J. & BRENNER, H. 1983 *Low Reynolds Number Hydrodynamics: with Special Applications to Particulate Media*, vol. 1. Springer.
- KHALILI, A. & LIU, B. 2017 Stokes' paradox: creeping flow past a two-dimensional cylinder in an infinite domain. *J. Fluid Mech.* **817**, 374–387.
- LAUGA, E. & ELOY, C. 2013 Shape of optimal active flagella. *J. Fluid Mech.* **730**, R1.
- LIU, R., ZHU, H., GUO, H., BONNET, M. & VEERAPANENI, S. 2025 Shape optimization of slip-driven axisymmetric microswimmers. *SIAM J. Sci. Comput.* **47** (2), A1065–A1090.
- MITCHELL, W.H. & SPAGNOLIE, S.E. 2017 A generalized traction integral equation for stokes flow, with applications to near-wall particle mobility and viscous erosion. *J. Comput. Phys.* **333**, 462–482.
- MOFFATT, H.K. 1964 Viscous and resistive eddies near a sharp corner. *J. Fluid Mech.* **18** (1), 1–18.
- MONTENEGRO-JOHNSON, T.D. & LAUGA, E. 2015 The other optimal Stokes drag profile. *J. Fluid Mech.* **762**, R3.
- MUSKHELISHVILI, N.I. 1977 *Some Basic Problems of the Mathematical Theory of Elasticity*. Springer.
- NIJER, J., LI, C., KOTHARI, M., HENZEL, T., ZHANG, Q., TAI, J.-S.B., ZHOU, S., COHEN, T., ZHANG, S. & YAN, J. 2023 Biofilms as self-shaping growing nematics. *Nat. Phys.* **19** (12), 1936–1944.
- PEARCE, P., SONG, B., SKINNER, D.J., MOK, R., HARTMANN, R., SINGH, P.K., JECKEL, H., OISHI, J.S., DRESCHER, K. & DUNKEL, J. 2019 Flow-induced symmetry breaking in growing bacterial biofilms. *Phys. Rev. Lett.* **123** (25), 258101.
- PIRONNEAU, O. 1973 On optimum profiles in Stokes flow. *J. Fluid Mech.* **59** (1), 117–128.
- POZRIKIDIS, C. 1992 *Boundary Integral and Singularity Methods for Linearized Viscous Flow*. Cambridge University Press.
- PROUDMAN, I. & PEARSON, J.R.A. 1957 Expansions at small Reynolds numbers for the flow past a sphere and a circular cylinder. *J. Fluid Mech.* **2** (3), 237–262.
- RICHARDSON, S. 1995 Optimum profiles in two-dimensional Stokes flow. *Proc. Roy. Soc. A* **450**(1940), 603–622.
- ROPER, M., PEPPER, R.E., BRENNER, M.P. & PRINGLE, A. 2008 Explosively launched spores of ascomycete fungi have drag-minimizing shapes. *Proc. Natl Acad. Sci.* **105** (52), 20583–20588.
- SHINTANI, K., UMEMURA, A. & TAKANO, A. 1983 Low-Reynolds-number flow past an elliptic cylinder. *J. Fluid Mech.* **136**, 277–289.
- TAKAISI, Y. 1955 The drag on a circular cylinder moving with low speeds in a viscous liquid between two parallel walls. *J. Phys. Soc. Japan* **10** (8), 685–693.
- TAKAISI, Y. 1956 The drag on a circular cylinder placed in a stream of viscous liquid midway between two parallel planes. *J. Phys. Soc. Japan* **11** (10), 1092–1095.
- TAVAKOL, B., FROELICHER, G., HOLMES, D.P. & STONE, H.A. 2017 Extended lubrication theory: improved estimates of flow in channels with variable geometry. *Proc. Roy. Soc. A* **473** (2206), 20170234.
- YU, D.-G., GONG, W., ZHOU, J., LIU, Y., ZHU, Y. & LU, X. 2024 Engineered shapes using electrohydrodynamic atomization for an improved drug delivery. *Wiley Interdiscip. Rev.: Nanomed. Nanobiotechnol.* **16** (3), e1964.
- ZABARANKIN, M. 2013 Minimum-resistance shapes in linear continuum mechanics. *Proc. Roy. Soc. A* **469** (2160), 20130206.
- ZABARANKIN, M. & NIR, A. 2011 Generalized analytic functions in an extensional stokes flow with a deformable drop. *SIAM J. Appl. Math.* **71** (4), 925–951.
- ZHANG, Q., LI, J., NIJER, J., LU, H., KOTHARI, M., ALERT, R., COHEN, T. & YAN, J. 2021 Morphogenesis and cell ordering in confined bacterial biofilms. *Proc. Natl Acad. Sci.* **118** (31), e2107107118.